RMetS

Royal Meteorological Society

An inherently mass-conserving iterative semi-implicit semi-Lagrangian discretization of the non-hydrostatic vertical-slice equations

Thomas Melvin,* Mark Dubal, Nigel Wood, Andrew Staniforth and Mohamed Zerroukat

Met Office, Exeter, UK
*Correspondence to: Thomas Melvin, Met Office, FitzRoy Road, Exeter EX1 3PB, UK. E-mail: Thomas.Melvin@metoffice.gov.uk

Recently an inherently mass-conserving semi-Lagrangian transport scheme has been successfully coupled to an iterative semi-implicit scheme in a global shallow-water-equation (SWE) model. Here that methodology is extended and applied to an iterative semi-implicit semi-Lagrangian (SISL) compressible, non-hydrostatic vertical-slice model, in which the constant reference state of the SWE model is now replaced by a vertically varying reference state. An advantage of this approach is that it preserves the same basic structure as the interpolating, non-mass-conserving, iterative SISL model. The resulting mass-conserving model is applied to a standard set of test problems for such models and compared with results from both the literature and the interpolating, iterative SISL version of the model. © Crown Copyright 2010. Reproduced with the permission of HMSO. Published by John Wiley & Sons, Ltd.

1. Introduction

There are two important aspects of semi-implicit semi-Lagrangian (SISL) models that make inherent, discrete conservation of mass difficult to achieve.

The first is the long-standing, well-known problem that the interpolation of a quantity to a departure point (in the context of a backward trajectory scheme) will not, in general, preserve the appropriate volume integral of that quantity. A number of schemes have been developed over recent years that address this issue in the context of passive transport (Zerroukat *et al.*, 2002, and references therein). Most of these achieve conservation by employing a finite-volume semi-Lagrangian approach, together with some conservative remapping algorithm applied to the integrals over the departure volume (see, for example, the review of Machenhauer *et al.*, 2008).

The second is that for models employing time steps of the size that a semi-Lagrangian discretization permits it is important that the divergence of the wind is discretized in such a way that the fast waves are handled stably. This is particularly important in compressible non-hydrostatic models, since these admit acoustic waves which, for practical values of the time step, are almost always unresolved in time. Here the target discretization is a semi-implicit one, though there are alternatives, such as the closely related, time-staggered regularized approach of Reich *et al.* (2007).

In addressing the first issue, it is usual for the Eulerian form of the continuity equation for density to be replaced by an advection equation for the mass. This removes the explicit appearance of the wind divergence term from the equation set and therefore makes the second aspect difficult to achieve. A particular method of overcoming this problem, in the context of a shallow-water-equation (SWE) model, has been recently presented in Zerroukat *et al.* (2009) (other

related approaches such as those of Lauritzen *et al.* (2006, 2008) and Kaas (2008) are discussed therein). This involves introducing a reference state (in fact a reference constant in the context of a SWE model) into the continuity equation, thereby making a wind divergence term materialize in such a way that it can be handled in a mass-conserving manner.

A SWE model is a useful test bed for many aspects of a full three-dimensional model, since it admits Rossby and external gravity wave propagation as well as the response of such waves to orographic forcing. However, such a model does not test how discretization handles the propagation of internal gravity and acoustic waves (as appropriate for a compressible non-hydrostatic model) nor does it test the influence of a terrain-following vertical coordinate in the presence of orography. In contrast, a compressible, non-hydrostatic vertical-slice model (here a Cartesian $x–z$ model) does admit these features. As a result, a vertical-slice model is complementary to a SWE model and is a crucial component of a hierarchy of prototypical models, which ultimately leads to a compressible, non-hydrostatic three-dimensional model.

Therefore, the methodology used by Zerroukat *et al.* (2009) to incorporate a mass-conserving semi-Lagrangian scheme into a semi-implicit discretization of the SWE is here extended to the discretization of the compressible, non-hydrostatic vertical-slice equations in Cartesian geometry. Note that here the term semi-implicit is used in the sense of Côté *et al.* (1998) and Zerroukat *et al.* (2009) to denote the averaging of terms over the implicit time level $n + 1$ and the explicit time level n. These methods are often referred to as centred-implicit methods and, as presented here, as iterative-centred-implicit methods. The equation set, the extraction of an appropriate reference profile and the handling of the orography via the usual terrain-following coordinate are all detailed in section 2. Those equations, both in mass-conserving and standard interpolating form, are discretized in a SISL manner in section 3. In addition to the mass-conserving property (here achieved by application of the PSM−SLICE scheme of Zerroukat *et al.*, 2007), the model combines a number of other distinguishing features.

- The Coriolis terms are discretized following Thuburn and Staniforth (2004) but extended to the nonlinear, deep-atmosphere case.
- The near boundary correction of Wood *et al.* (2009) is applied to prevent departure points lying spuriously at or beyond a physical boundary, thereby preventing the occurrence of vanishing control volumes.
- Following Girard *et al.* (2005), a semi-Lagrangian discretization of the relation between the vertical motion, $\dot{\eta}$, of the transformed coordinate and the actual vertical velocity, w, is used.
- Following Côté *et al.* (1998) and Zerroukat *et al.* (2009), a multiply-nested iterative approach is used to solve the equation set, thereby avoiding any three-time-level extrapolations (so that the model is a truly two-time-level one). Therefore at convergence, and for the values of 1/2 used here for the off-centring parameters, the discretization is centred and second-order accurate.
- Motivated by the results of the Klemp *et al.* (2008) study, an implicit Rayleigh damping layer has been applied to the w equation, thereby using one of the two damping mechanisms introduced by Klemp *et al.*

(2008): this is used, where appropriate, to control the spurious reflection of vertically propagating waves from the rigid lid.

The resulting mass-conserving model is applied to a standard set of test cases in section 4, and compared with results from the interpolating, non-mass-conserving, SISL version and also with results from the literature. Finally, conclusions are drawn in section 5.

2. Governing equations

2.1. Height coordinates

The two-dimensional dry Euler equations in Cartesian $x–z$ coordinates are considered. Thuburn and Woollings (2005) show that optimal discrete dispersion properties for these equations can be obtained by, for example, writing the pressure gradient term in the form $c_p\theta\nabla\pi$ (with subsequent appropriate discretization). Furthermore, to facilitate the discrete conservation of mass, density is retained as a prognostic variable. Consistent with these constraints the equation set is chosen to be (cf. Davies *et al.*, 2005; Shin and Reich, 2009)

$$\frac{Du}{Dt} + c_p\theta\frac{\partial\pi}{\partial x} - fv + Fw = 0, \tag{1}$$

$$\frac{Dv}{Dt} + fu = 0, \tag{2}$$

$$\delta_V\frac{Dw}{Dt} + c_p\theta\frac{\partial\pi}{\partial z} + g - Fu = 0, \tag{3}$$

$$\frac{D}{Dt}\left(\int_{\delta\mathcal{A}}\rho\,d\mathcal{A}\right) = 0, \tag{4}$$

$$\frac{D\theta}{Dt} = 0, \tag{5}$$

$$\pi^{(1-\kappa)/\kappa} = \frac{R}{p_0}\rho\theta, \tag{6}$$

where

$$\pi \equiv \left(\frac{p}{p_0}\right)^\kappa, \tag{7}$$

$$f \equiv 2\Omega\sin\phi, \qquad F \equiv 2\Omega\cos\phi, \tag{8}$$

and

$$\frac{D}{Dt} \equiv \frac{\partial}{\partial t} + u\frac{\partial}{\partial x} + w\frac{\partial}{\partial z} \tag{9}$$

is the total derivative following the fluid. Also, u, v and w are the three components of the velocity vector, θ is potential temperature, ρ is density, π is Exner pressure, p is pressure, p_0 is a constant reference pressure, R is the gas

constant, c_p is the specific heat at constant pressure and $\kappa \equiv R/c_p$. Equations (1)–(6) are the three components of the momentum equation, the continuity equation, the thermodynamic equation and the equation of state, respectively.

While the equations admit flow (v) in the third, y direction, they are two-dimensional in the sense that no gradients of prognostic variables are admitted in the y direction.

An $f-F$ plane approximation is assumed in which the equations are solved on a plane that is tangent to the sphere at a particular constant latitude ϕ. Then the Coriolis parameters f and F are fixed at their values at that latitude (Beckmann and Diebels, 1994; Thuburn *et al.*, 2002). For all the standard examples presented later (see section 4) the further approximation to an f-plane is made, i.e. $F \equiv 0$.

A quasi-hydrostatic switch, δ_V, has been introduced into the vertical momentum equation (3), such that the equation set is fully compressible when $\delta_V \equiv 1$ but reduces to the quasi-hydrostatic equation set (White *et al.*, 2005) when $\delta_V \equiv 0$.

Equation (4) is the integral equivalent of the more usual differential form

$$\frac{D\rho}{Dt} + \rho \mathfrak{D} = 0 \qquad (10)$$

of the continuity equation used in traditional SISL discretizations, where

$$\mathfrak{D} \equiv \frac{\partial u}{\partial x} + \frac{\partial w}{\partial z}. \qquad (11)$$

The integral in (4) is over the (finite) material volume, $\delta \mathcal{A}$ (this is an area here as only two dimensions are considered), which moves with the fluid.

The Lagrangian integral form (4) of the continuity equation is well suited for a conserving semi-Lagrangian discretization (see e.g. Zerroukat *et al.* (2002) for the use of this form for conservative passive tracer transport). However, in order to apply a semi-implicit scheme and thereby couple the mass field stably to the wind field, the divergence field needs to be discretized implicitly, since it controls the propagation of fast acoustic and gravity waves. In its present form (4) the divergence field does not explicitly appear. It is only implied through the trajectory equations, since they determine the departure area. In order to make the divergence field materialize, the approach of Zerroukat *et al.* (2009) is followed in which a reference profile, ρ^{ref}, is introduced. Here the procedure is complicated by the fact that, in contrast to the case of the shallow-water equations of Zerroukat *et al.* (2009), ρ^{ref} is not simply a constant but can vary spatially. Appendix A gives details of the derivation with the result that (4) can be rewritten as

$$\frac{D}{Dt}\left[\int_{\delta \mathcal{A}}\left(\rho - \rho^{\mathrm{ref}}\right) \mathrm{d}\mathcal{A}\right] + \int_{\delta \mathcal{A}} \nabla \cdot \left(\rho^{\mathrm{ref}}\mathbf{u}\right) \mathrm{d}\mathcal{A} = 0, \qquad (12)$$

where it has been assumed that ρ^{ref} is stationary in time, varying only in space.

Similarly, and as shown in appendix A, (5) can be rewritten as

$$\frac{D\left(\theta - \theta^{\mathrm{ref}}\right)}{Dt} + \mathbf{u} \cdot \nabla \theta^{\mathrm{ref}} = 0. \qquad (13)$$

This form is the standard semi-implicit method of rewriting the advection of thermodynamic variables, to allow the coupling between the thermodynamic and vertical velocity equations to be handled implicitly.

2.2. Terrain-following coordinates

To incorporate orography, the equations are transformed into a terrain-following vertical coordinate, $\eta = \eta(x, z)$, which is independent of time. The transformation is assumed to be monotonic, i.e. $\partial z/\partial \eta$ is non-zero and single-signed and $\eta = 0$ corresponds to the lower boundary, $z = z_S(x)$, and $\eta = 1$ to the upper boundary, $z = z_T = \mathrm{constant}$. The velocity components u, v and w retain their original form. Additionally the reference profiles are now assumed to be a function only of η.

Details of the transformation relations are given in appendix B. Using these relations, the governing equations (1)–(3), (12), (13) and (6) become

$$\frac{Du}{Dt} = \Psi_u$$
$$\equiv -\frac{c_p\theta}{\partial z/\partial \eta}\left[\frac{\partial}{\partial x}\left(\pi \frac{\partial z}{\partial \eta}\right) - \frac{\partial}{\partial \eta}\left(\pi \frac{\partial z}{\partial x}\right)\right]$$
$$+ fv - Fw, \qquad (14)$$

$$\frac{Dv}{Dt} = \Psi_v \equiv -fu, \qquad (15)$$

$$\delta_V \frac{Dw}{Dt} = \Psi_w \equiv -\frac{c_p\theta}{\partial z/\partial \eta}\frac{\partial \pi}{\partial \eta} - g + Fu, \qquad (16)$$

$$\frac{D}{Dt}\left[\int_{\delta \mathcal{A}}\left(\rho - \rho^{\mathrm{ref}}\right) \mathrm{d}\mathcal{A}\right] + \int_{\delta \mathcal{A}} \nabla \cdot \left(\rho^{\mathrm{ref}}\mathbf{u}\right) \mathrm{d}\mathcal{A} = 0, \qquad (17)$$

$$\frac{D}{Dt}\left(\theta - \theta^{\mathrm{ref}}\right) + \mathbf{u} \cdot \nabla \theta^{\mathrm{ref}} = 0 \qquad (18)$$

and

$$\pi^{(1-\kappa)/\kappa} = \frac{R}{p_0}\rho\theta, \qquad (19)$$

where now

$$\frac{D}{Dt} \equiv \frac{\partial}{\partial t} + u\frac{\partial}{\partial x} + \dot{\eta}\frac{\partial}{\partial \eta}, \qquad (20)$$

$$\nabla \cdot \left(\rho^{\mathrm{ref}}\mathbf{u}\right) = \left(\frac{\partial z}{\partial \eta}\right)^{-1}$$
$$\times \left[\frac{\partial}{\partial x}\left(\rho^{\mathrm{ref}}\frac{\partial z}{\partial \eta}u\right) + \frac{\partial}{\partial \eta}\left(\rho^{\mathrm{ref}}\frac{\partial z}{\partial \eta}\dot{\eta}\right)\right] \qquad (21)$$

and partial derivatives with respect to x are taken holding η, rather than z, constant.

To close the formulation, zero mass flux is assumed at the lower and upper boundaries, so that $\dot{\eta} \equiv 0$ there.

In anticipation of a semi-Lagrangian discretization, the trajectory equations are

$$\frac{Dx}{Dt} \equiv u, \qquad \frac{D\eta}{Dt} \equiv \dot{\eta}. \qquad (22)$$

The vertical velocity, w, is related to the vertical motion, $\dot{\eta}$, as defined in (22), by

$$\dot{\eta} \equiv \frac{D\eta}{Dt} = \left(\frac{\partial z}{\partial \eta}\right)^{-1}\left(w - \left.\frac{Dz}{Dt}\right|_\eta\right), \tag{23}$$

where $(Dz/Dt)|_\eta$ is the rate of change of height of a particle due to the action of the horizontal velocity if that particle were constrained to remain on a surface of constant η (see (B10) in appendix B). The two-dimensional Eulerian representation of $(Dz/Dt)|_\eta$ is $u\partial z/\partial x$ (cf. (B6) of appendix B).

3. Discretization

3.1. Discrete equations

The governing equations are discretized in time using a two-time-level SISL scheme. A staggered Arakawa-C grid is used in the horizontal and a Charney–Phillips grid in the vertical. Davies *et al.* (2005) discuss the merits of, and motivation for, such a combination, aspects of which are supported by the analysis of Thuburn and Woollings (2005). Relevant terms in the governing equations are then discretized using two-point differencing and averaging operators. Appendix C gives details of the variable placement and spatial operators. The resulting discrete equations are given below.

In what follows, α determines the spatio–temporal off-centring along the trajectory ($\alpha = 1/2$ corresponds to centring along the trajectory), $\beta \equiv 1 - \alpha$ and subscripts A and D denote evaluation at an arrival and departure point, respectively or, for an integral quantity as in (30), at an arrival and departure cell, respectively.

3.1.1. Momentum equations (14)–(16)

$$(u - \alpha\Delta t\Psi_u)_A^{n+1} = R_u^n \equiv (u + \beta\Delta t\Psi_u)_D^n, \tag{24}$$

$$(v - \alpha\Delta t\Psi_v)_A^{n+1} = R_v^n \equiv (v + \beta\Delta t\Psi_v)_D^n, \tag{25}$$

$$[(\delta_V + \mu\Delta t)w - \alpha\Delta t\Psi_w]_A^{n+1} = R_w^n$$
$$\equiv (\delta_V w + \beta\Delta t\Psi_w)_D^n, \tag{26}$$

where

$$\Psi_u = \frac{1}{\Delta x}\left\langle fv\Delta x - \langle\Delta x\overline{\rho}^\eta w\rangle^\eta \frac{F}{\rho}\right\rangle^x$$
$$- \frac{c_p\overline{\theta}^{x\eta}}{(\delta_\eta z)}\{\delta_x(\pi\delta_\eta z) - \delta_\eta[\overline{\pi}^{x\eta}(\delta_x z)]\}, \tag{27}$$

$$\Psi_v = -\frac{f}{\Delta\eta(\delta_\eta z)\rho}\langle\Delta\eta(\delta_\eta z)\overline{\rho}^x u\rangle^x \tag{28}$$

and

$$\Psi_w = \frac{1}{\Delta\eta(\delta_\eta z)}\left\langle\langle\Delta\eta(\delta_\eta z)\overline{\rho}^x u\rangle^x \frac{F}{\rho}\right\rangle^\eta - \frac{c_p\theta}{(\delta_\eta z)}\delta_\eta\pi - g. \tag{29}$$

To obtain good Rossby-mode dispersion properties, the Coriolis terms in (27)–(29) have been discretized following the linear shallow-water scheme described in Thuburn and Staniforth (2004) but extended here to the nonlinear deep-atmosphere case.

An absorbing layer has now been added to prevent spurious reflection of vertically propagating waves from the model lid. Motivated by the results of Klemp *et al.* (2008), this is achieved by adding a single damping term $-\mu w$ to the right-hand side of the w-equation (3), which is then time-discretized in a fully implicit manner. This results in the appearance of the term involving μw_A^{n+1} on the left-hand side of (26). The specification of $\mu = \mu(\eta)$ is case-dependent and is discussed in section 4. Following Temam and Tribbia (2003), this damping term is formulated so that it is active in the hydrostatic mode, $\delta_V = 0$. This means that in the sponge layer, where $\mu \neq 0$, hydrostatic balance will not be strictly enforced.

3.1.2. Continuity equation (17)

$$\left[(\rho - \rho^{ref}) + \alpha\Delta t\nabla\cdot(\rho^{ref}\mathbf{u})\right]_A^{n+1} = R_\rho^n$$
$$\equiv \frac{1}{\Delta\mathcal{A}}\left\{\int_{\delta\mathcal{A}}\left[(\rho - \rho^{ref}) - \beta\Delta t\nabla\cdot(\rho^{ref}\mathbf{u})\right]d\mathcal{A}\right\}_D^n, \tag{30}$$

where

$$\nabla\cdot(\rho^{ref}\mathbf{u})$$
$$= \frac{\Delta x\Delta\eta}{\Delta\mathcal{A}}\left\{\delta_x\left[(\delta_\eta z)\rho^{ref}u\right] + \delta_\eta\left[(\delta_\eta z)\overline{\rho^{ref}}^\eta\dot{\eta}\right]\right\} \tag{31}$$

and

$$\Delta\mathcal{A} = (\delta_\eta z)\Delta x\Delta\eta. \tag{32}$$

The divergence term (31) is discretized in a conservative flux form. Therefore, provided the integral over the departure area, required for the evaluation of R_ρ^n, is conservative, (30) ensures that the discrete volume integral of ρ is conserved. Any conservative remapping algorithm can be used for the evaluation of R_ρ^n; here the SLICE algorithm of Zerroukat *et al.* (2002) using the Parabolic Spline Method of Zerroukat *et al.* (2006) is adopted (without its monotonicity filter).

3.1.3. Thermodynamic equation (18)

$$\left[(\theta - \theta^{ref}) + \alpha\Delta t\dot{\eta}\delta_\eta(\overline{\theta^{ref}}^\eta)\right]_A^{n+1} = R_\theta^n$$
$$\equiv \left[(\theta - \theta^{ref}) - \beta\Delta t\dot{\eta}\delta_\eta(\overline{\theta^{ref}}^\eta)\right]_D^n. \tag{33}$$

3.1.4. Equation of state (19)

$$\pi^{(1-\kappa)/\kappa} = \left(\frac{R}{p_0}\right)\rho\overline{\theta}^\eta. \tag{34}$$

3.1.5. Kinematic equations (22)

$$x_D^n = x_A^{n+1} - \left[\alpha_x u_A^{n+1} + \beta_x u^n(x_D^n, \eta_D^n)\right]\Delta t, \tag{35}$$

$$\eta_D^n = \eta_A^{n+1} - \left[\alpha_x \dot{\eta}_A^{n+1} + \beta_x \dot{\eta}^n \left(x_D^n, \eta_D^n\right)\right] \Delta t, \qquad (36)$$

where α_x is a spatio–temporal off-centring parameter analogous to α, with $\beta_x \equiv 1 - \alpha_x$ and $\alpha_x = 1/2$ corresponding to trajectory centring. Since the right-hand sides of (35)–(36) depend on the left-hand-side values, these equations are solved iteratively. If, during an iteration, the departure point lies below the first, or above the last, internal model level then its position is corrected following the procedure of Wood *et al.* (2009), thereby avoiding any vanishingly thin departure layers.

3.1.6. *Vertical motion equation* (23)

Schär *et al.* (2002) investigated the sensitivity of model simulations of flow over fine-scale orography to the form of the terrain-following coordinate employed. Klemp *et al.* (2003) identified that poor results can arise due to inconsistent handling (and therefore lack of cancellation) of certain terms in the terrain-following coordinate system. Consistent with the analysis of Klemp *et al.* (2003), Girard *et al.* (2005) further showed that for semi-Lagrangian models the problem can be mitigated by discretizing (23) in a semi-Lagrangian manner, rather than in the more usual Eulerian manner. Their discretization of (23) is in the context of a three-time-level scheme. Therefore, inspired by their approach, (23) is discretized in a two-time-level context and centred along the trajectory, as

$$\begin{aligned}
\alpha_{\dot{\eta}} \left[\left(\delta_\eta z\right) \dot{\eta} - w\right]_A^{n+1} &= R_{\dot{\eta}}^n \\
&\equiv -\beta_{\dot{\eta}} \left[\left(\delta_\eta z\right) \dot{\eta} - w\right]_D^n \\
&\quad - \frac{\alpha_{\dot{\eta}} \left[z\left(x_A, \eta_A\right) - z\left(x_D, \eta_A\right)\right]}{\Delta t} \\
&\quad - \frac{\beta_{\dot{\eta}} \left[z\left(x_A, \eta_D\right) - z\left(x_D, \eta_D\right)\right]}{\Delta t},
\end{aligned}$$
$$(37)$$

with off-centring parameters $\alpha_{\dot{\eta}}$ and $\beta_{\dot{\eta}} \equiv 1 - \alpha_{\dot{\eta}}$.

3.1.7. *Boundary conditions*

To close the discrete problem, boundary conditions are needed at the top and bottom levels in addition to requiring that $\dot{\eta} = 0$ there. Computation of the departure points requires a value of the horizontal wind at the surface. To do this, the horizontal wind speed is assumed to be constant in the bottom and top half layers. This then allows (33) to be evaluated at the top and bottom surfaces (i.e. θ is passively advected along the top and bottom surfaces). In terrain-following coordinates, the evaluation of the pressure gradient term in (27) also requires an estimate of the surface pressure. Here this is obtained, at each inner loop iteration, by requiring the vertical momentum equation (26) to hold at the surface, thereby giving an estimate for $\partial \pi / \partial \eta|_{\eta=0}$. Then, consistent with the centred discretizations used for the rest of the model, π_0 is estimated from

$$\left.\frac{\partial \pi}{\partial \eta}\right|_{1/4} = \frac{\pi_{1/2} - \pi_0}{\eta_{1/2} - \eta_0} = \frac{\overline{\theta \left.\frac{\partial \pi}{\partial \eta}\right|}^{\eta}\Big|_{1/4}}{\overline{\theta}^{\eta}\Big|_{1/4}}, \qquad (38)$$

where subscripts denote evaluation at that level. This method has the advantage of recovering the natural estimates in both the hydrostatic and isentropic limits.

3.2. *Solution procedure*

Equations (24)–(26), (30) and (33)–(34), together with (37), form a set of nonlinear equations for u^{n+1}, v^{n+1}, w^{n+1}, ρ^{n+1}, θ^{n+1}, π^{n+1} and $\dot{\eta}^{n+1}$. Following Côté *et al.* (1998), these nonlinear equations are solved by iterating around a linear kernel that consists of a Helmholtz equation (derived in section 3.3). Within an outer iteration loop, the departure-point locations are updated using the latest available estimates of the winds at the next time step. Within the inner loop the nonlinear terms, together with the Coriolis terms, are evaluated using estimates of the prognostic variables obtained at the previous iteration. Appendix D gives further details of the iterative procedure.

In order to derive the linear kernel, all variables at time level $n + 1$ are written as (finite-amplitude) perturbations about stationary (i.e. $\mathbf{u}^{\mathrm{ref}} \equiv \mathbf{0}$) reference profiles. These profiles are those introduced in Section 2, supplemented by a reference pressure profile $\pi^{\mathrm{ref}}(\eta)$. For a generic variable, G, the decomposition is given by $G^{n+1} \equiv G^{\mathrm{ref}}(\eta) + G'$. The prime notation therefore implicitly has a time level $(n + 1)$ associated with it. Note that for the velocity components the reference profile is identically zero and therefore, for these components, $G' \equiv G^{n+1}$.

The nonlinear and Coriolis terms that are evaluated using values from the previous iteration are grouped together into variables of the generic form R_G^*.

3.2.1. *Setting the scene*

To set the scene for the derivation of a discrete Helmholtz problem, the discrete equation set (24)–(26), (30), (33), (37) and (34) is rewritten as follows:

$$u' + H_u \delta_x \left(\pi' \delta_\eta z\right) = R_u^* + R_u^n, \qquad (39)$$

$$v' = R_v^* + R_v^n, \qquad (40)$$

$$\left(\delta_V + \Delta t \mu\right) w' + H_w \left(\delta_\eta \pi^{\mathrm{ref}}\right) \frac{\theta'}{\theta^{\mathrm{ref}}} + H_w \delta_\eta \pi' \\
= R_w^* + R_w^n, \qquad (41)$$

$$\rho' + H_V \left[\delta_x \left(H_{\rho x} u'\right) + \delta_\eta \left(H_{\rho z} \dot{\eta}'\right)\right] = R_\rho^n, \qquad (42)$$

$$\theta' + H_\theta \dot{\eta}' = R_\theta^n, \qquad (43)$$

$$H_{\dot{\eta}} \dot{\eta}' - w' = R_{\dot{\eta}}^n, \qquad (44)$$

$$\frac{1-\kappa}{\kappa} \frac{\pi'}{\pi^{\mathrm{ref}}} - \overline{\left[\frac{\rho'}{\rho^{\mathrm{ref}}} + \overline{\left(\frac{\theta'}{\theta^{\mathrm{ref}}}\right)}^{\eta}\right]} = R_\pi^*, \qquad (45)$$

together with

$$\dot{\eta}' = 0 \qquad (46)$$

at the top and bottom bounding surfaces of the model. The R_G^* terms in (39)−(45) are

$$R_u^* \equiv \alpha \Delta t \left(\Psi_u\right)^{n+1} + H_u \delta_x \left(\pi' \delta_\eta z\right), \quad (47)$$

$$R_v^* \equiv \alpha \Delta t \left(\Psi_v\right)^{n+1}, \quad (48)$$

$$R_w^* \equiv \alpha \Delta t \left(\Psi_w\right)^{n+1} + H_w \left(\delta_\eta \pi^{\text{ref}}\right) \frac{\theta'}{\theta^{\text{ref}}} + H_w \delta_\eta \pi', \quad (49)$$

$$R_\pi^* \equiv \left[1 - \frac{p_0 \left(\pi^{n+1}\right)^{(1-\kappa)/\kappa}}{R \rho^{\text{ref}} \overline{\left(\theta^{n+1}\right)}^\eta}\right] + \frac{1-\kappa}{\kappa} \frac{\pi'}{\pi^{\text{ref}}} - \overline{\left(\frac{\theta'}{\theta^{\text{ref}}}\right)}^\eta, \quad (50)$$

and the subscripted H coefficients are defined in appendix E.

3.3. Helmholtz equation

At each inner iteration, a Helmholtz problem is solved for π' and the latest estimate of π^{n+1} is updated. The latest estimates of the prognostic variables are then obtained from the discretized equations by a process of back-substitution, and the R^* terms are updated. Algebraic elimination of u', v', w', ρ', θ' and $\dot{\eta}'$ from (39)−(45) with their R^* values held fixed and using (46) at the top and bottom boundaries leads to the discrete Helmholtz equation

$$H_V \delta_x \left[H_{\rho x} H_u \delta_x \left(\pi' \delta_\eta z\right)\right] + H_V D_1 \left[D_2 \left(\pi'\right)\right]$$
$$- \left(\frac{1-\kappa}{\kappa} \rho^{\text{ref}}\right) \frac{\pi'}{\pi^{\text{ref}}} = \mathfrak{R}^n + \mathfrak{R}^*, \quad (51)$$

where

$$D_1 \left(X\right) \equiv \delta_\eta \left(H_{\rho z} X\right) + \frac{1}{H_V} \rho^{\text{ref}} \overline{\left(\frac{H_\theta X}{\theta^{\text{ref}}}\right)}^\eta, \quad (52)$$

$$D_2 \left(X\right) \equiv H_w H_C \left(\delta_\eta X\right), \quad (53)$$

$$\mathfrak{R}^n \equiv -\rho^{\text{ref}} \overline{\left(\frac{R_\theta^n}{\theta^{\text{ref}}}\right)}^\eta - R_\rho^n + H_V \delta_x \left(H_{\rho x} R_u^n\right)$$
$$+ H_V D_1 \left\{H_C \left[R_w^n - \frac{H_w \left(\delta_\eta \pi^{\text{ref}}\right)}{\theta^{\text{ref}}} R_\theta^n\right.\right.$$
$$\left.\left. + \left(\delta_V + \Delta t \mu\right) R_\eta^n\right]\right\}, \quad (54)$$

$$\mathfrak{R}^* \equiv -\rho^{\text{ref}} R_\pi^* + H_V \delta_x \left(H_{\rho x} R_u^*\right) + H_V D_1 \left(H_C R_w^*\right), \quad (55)$$

with

$$H_C \equiv \left[\left(\delta_V + \Delta t \mu\right) H_{\dot{\eta}} - \frac{H_w \delta_\eta \pi^{\text{ref}}}{\theta^{\text{ref}}} H_\theta\right]^{-1}. \quad (56)$$

The coefficients on the left-hand side of (51) (i.e. the H values and thermodynamic reference profiles) are invariant in time. The right-hand side of (51) contains both explicitly known terms (i.e. the R^n) and implicitly defined nonlinear (and Coriolis) terms (i.e. the R^*), which are updated in the inner loop. As part of the back-substitution process, $\dot{\eta}'$ is obtained from π' using

$$\dot{\eta}' + D_2 \left(\pi'\right) = H_C \left[R_w^* + R_w^n + \left(\delta_V + \Delta t \mu\right) R_\eta^n\right.$$
$$\left. - \frac{H_w \delta_\eta \pi^{\text{ref}}}{\theta^{\text{ref}}} R_\theta^n\right]. \quad (57)$$

This equation results from the algebraic elimination of w' and θ' from (41), (43) and (44).

3.4. Interpolating SISL version of the model

To facilitate validation of the model, a version has been created that differs only in its use of an interpolating SISL discretization of the continuity equation (10). Following Zerroukat *et al.* (2009), this is referred to as the standard version. Thus the discretization (30) of (17) is replaced by the discretization

$$\left[\left(\rho - \rho^{\text{ref}}\right) + \alpha \Delta t \nabla \cdot \left(\rho^{\text{ref}} \mathbf{u}\right)\right]^{n+1} = R_\rho^* + R_\rho^n \quad (58)$$

of (10), where R_ρ^n is redefined to be

$$R_\rho^n \equiv \left[\left(\rho - \rho^{\text{ref}}\right) - \beta \Delta t \nabla \cdot \left(\rho^{\text{ref}} \mathbf{u}\right)\right.$$
$$\left. - \beta \Delta t \left(\rho - \rho^{\text{ref}}\right) \nabla \cdot \mathbf{u}\right]_D^n, \quad (59)$$

and R_ρ^* is defined to be

$$R_\rho^* \equiv -\alpha \Delta t \left(\rho - \rho^{\text{ref}}\right) \nabla \cdot \mathbf{u}. \quad (60)$$

Since (58) has the same form as (30), except for the extra term R_ρ^*, the solution procedure described above goes through virtually unchanged. The only real difference in the procedure is that the $\mathfrak{R}^*$ term in (51), as defined in (55), has an additional contribution, $-R_\rho^*$, which is evaluated in the inner loop with the other contributions to $\mathfrak{R}^*$. The resulting version of the model corresponds to a two-time-level, fully interpolating discretization of the fully compressible, inviscid vertical-slice equations on an $f - F$ plane.

4. Computational examples

The test cases presented here are taken from a standard set of test problems for 2D vertical-slice dynamical cores available at http://box.mmm.ucar.edu/projects/srnwp_tests/index.html. This suite of problems tests a variety of salient aspects of a vertical-slice model: self-advection; acoustic and gravity-wave propagation; buoyancy-driven flow; orographically driven flow; flow in both the hydrostatic and non-hydrostatic regimes.

In cases where orography is present, the linear transformation between the physical height, *z*, and the

terrain-following coordinate, η, used here, is of the form

$$\eta = \frac{z - z_S(x)}{z_T - z_S(x)}, \qquad (61)$$

where $z_S(x)$ is the orographic profile and $z_T = \text{constant}$ is the domain height. For all simulations, centred discretizations along the trajectories are used, i.e $\alpha = \beta = \alpha_x = \beta_x = \alpha_{\dot\eta} = \beta_{\dot\eta} = 1/2$.

Two iterations of both the inner nonlinear loop and the outer departure-point loop are also used; see appendix D for details of the iterative procedure. All results presented here used two inner and two outer loop iterations, with no visible benefit found from increasing the iterations to convergence.

The lateral boundary conditions consist of periodicity. As a result, in some cases the lateral domain size has been increased from that given in the original test descriptions: this is to reduce the impacts of 'outgoing' waves returning into the domain of interest.

The vertical boundary conditions are $\dot\eta = 0$ at $\eta = 0$ and 1. The upper boundary condition implies a rigid, reflecting lid. Where this causes problems for orographically forced flow, the sponge layer is used to reduce the impact of reflections from the upper boundary. The application of the sponge layer is implemented gradually from the base of the sponge layer, $\eta_B < 1$, to the top of the domain using the formula

$$\mu(\eta) = \begin{cases} 0, & \eta < \eta_B, \\ \overline{\mu}\sin^2\left[\frac{\Pi}{2}\left(\frac{\eta - \eta_B}{1 - \eta_B}\right)\right], & \eta \geq \eta_B, \end{cases} \qquad (62)$$

and $\overline{\mu}$ is a constant that is set appropriately for each application.

Since the reference profiles are a function of η only, they are obtained by first analytically specifying as appropriate the vertical profile $\theta^{\text{ref}}(\eta)$ in the absence of orography, and then sampling it on the model levels where θ is stored. Then π^{ref} is obtained by requiring discrete hydrostatic balance to hold, again in the absence of orography, i.e. by solving

$$\delta_\eta \pi^{\text{ref}} \equiv -\frac{g\left(\delta_\eta z\right)^{\text{ref}}}{c_p \theta^{\text{ref}}}, \qquad (63)$$

where $\left(\delta_\eta z\right)^{\text{ref}}$ is here taken to be z_T, the value of $\left(\delta_\eta z\right)$ in the absence of orography. Finally, ρ^{ref} is obtained by requiring the discrete equation of state to hold, i.e.

$$\rho^{\text{ref}} \equiv \frac{p_0\left(\pi^{\text{ref}}\right)^{(1-\kappa)/\kappa}}{R\overline{\theta^{\text{ref}}}^\eta}. \qquad (64)$$

The profile θ^{ref} is specified to be that appropriate for a constant buoyancy frequency (N) atmosphere, where $N^2 \equiv (g/\theta)\,\partial\theta/\partial z$. This includes the two special cases of isentropic ($\theta = \text{constant}$) and isothermal ($T \equiv \theta\pi = \text{constant}$) atmospheres.

The initial conditions for the thermodynamic variables are obtained in a very similar manner to the reference profiles. The key difference is that, where it occurs, $\delta_\eta z$ takes on its local value, dependent on the orography. Also, the solution for π is obtained by integrating the equivalent of (63) (extended to include the Coriolis term if appropriate)

down from the top of the model where, due to the fact that the model top is flat, a constant upper value of π is specified. Whilst this procedure imposes exact discrete hydrostatic balance in each column, it does not attempt to impose balance in the horizontal. The winds are set equal to their specified, undisturbed, values everywhere. The model therefore sees any orography impulsively and has to adjust to it. Additionally, where appropriate, a perturbation (e.g. to the potential temperature) is added to the stationary, hydrostatically balanced component to create the actual initial fields.

For comparison purposes, the values of the various parameters (with the exception of the domain size) have been chosen to be consistent with those used by previous authors. The resulting common settings of various parameters for all the illustrative examples are listed in Table I. The reference profiles π^{ref}, ρ^{ref}, θ^{ref} assume the same functional form for N as the initial states without any perturbations. They also have the same surface values but do not take any account of orography so that they are a function of η only, as stated in section 3.2. In the absence of orography, the unperturbed initial profiles and reference profiles are equivalent.

Note that, following other authors, generally in the figures of this section only the regions of interest are shown.

4.1. Gravity waves

This test case is described in Skamarock and Klemp (1994) and simulates the evolution of a potential temperature perturbation

$$\theta' = \Delta\theta_0 \frac{\sin\left(\Pi z/H\right)}{1 + (x - x_c)^2/a^2}, \qquad (65)$$

superimposed on a background atmospheric state with constant buoyancy frequency $N = 0.01\,\text{s}^{-1}$. In both the hydrostatic and non-hydrostatic flow regimes, a domain height of $H = 10\,\text{km}$ and a θ perturbation $\Delta\theta_0 = 10^{-2}\,\text{K}$, centred on $x_c = 0$, are used and a mean horizontal wind $U = 20\,\text{m\,s}^{-1}$ is imposed. This mean wind is balanced (in the presence of a non-zero Coriolis force) by imposing an appropriate pressure gradient force on the v-component of the momentum equation. For the hydrostatic flow regime, the width of the perturbation is determined from $a = 100\,\text{km}$ and the Coriolis parameter is set to $f = 10^{-4}\,\text{s}^{-1}$. In the non-hydrostatic flow regime, $a = 5\,\text{km}$ and there is no Coriolis force.

Skamarock and Klemp (1994) present solutions of a Boussinesq model, for both hydrostatic and non-hydrostatic flow regimes, and find good agreement between numerical and linear analytic solutions. Simulations of the full compressible equation set are presented in Hundertmark and Reich (2007), and also in the standard test documentation (available on the website given above) for the WRF and ARPS models. Whilst there are some differences in the solutions of the compressible equation set, most noticeably in the ARPS results, the overall agreement between models is good. However, in contrast to the Boussinesq results, including the effects of compressibility leads to solutions that are asymmetric about the line $z = H/2$.

Results for the hydrostatic and non-hydrostatic flow regimes are shown in Figures 1 and 2, respectively. The non-hydrostatic mass-conserving (Figures 1(b) and 2(b))

Table I. Model parameters for each test. Identifiers: HIGW −hydrostatic inertia−gravity waves; NHGW −non-hydrostatic gravity waves; DC −density current; HMW −hydrostatic mountain waves; NHMW −non-hydrostatic mountain waves; SH −Schär Hill test. The horizontal Courant number is given by $C_x \equiv U\Delta t/\Delta x$: for cases where $U = 0$, C_x has been calculated using the largest value of u'. For all cases the surface pressure (away from, or in the absence of, orography) is $$p_{surf} = 1000\,hPa \Rightarrow \pi_{surf} = 1.$$

Test	Δx (km)	Δz (m)	Δt (s)	Domain (km×km)	Background initial state	T_{surf} (K)	U (m s^{-1})	C_x
HIGW	10	500	100	6000×10	$N = 0.01\,s^{-1}$	300	20	0.2
NHGW	1	1000	12	300×10	$N = 0.01\,s^{-1}$	300	20	0.24
DC	0.05−0.2	50−200	0.5−4	51.2 × 6.4	Isentropic $\theta = T_{surf}$	300	0	≈ 0.4
HMW	2	250	20	240 × 50	Isothermal $T = T_{surf}$	250	20	0.2
NHMW	0.4	250	5	144×35	$N = 0.01\,s^{-1}$	300	10	0.125
SH	0.5	300	8	100×30	$N = 0.01\,s^{-1}$	288	10	0.16

and standard SISL (Figures 1(c) and 2(c)) models both give visually indistinguishable results for both hydrostatic and non-hydrostatic flow regimes. These results are in good agreement with other published results (see, for example, Hundertmark and Reich (2007) and the standard test set documentation). Figure 1(d) shows the result of applying the hydrostatic switch ($\delta_V = 0$) in the mass-conserving model to the case of the hydrostatic flow regime. It is seen that, compared with the case $\delta_V = 1$ (Figure 1(b)), there is a small variation in the maximum/minimum values, with the maximum value in hydrostatic mode being approximately 3% larger than in non-hydrostatic mode ($\delta_V = 1$), and the minimum value being also slightly larger than in the non-hydrostatic mode. It would seem that even at these scales there is a small effect due to the non-hydrostatic dynamics.

4.2.   Density current

This test simulates the evolution of a perturbation to the initial temperature field in the form of a cold bubble defined by Straka *et al.* (1993) to be

$$\Delta T = \begin{cases} 0 & \text{if } L_r > 1, \\ -15\left[\cos\left(\Pi L_r\right) + 1\right]/2 & \text{if } L_r \leq 1, \end{cases} \quad (66)$$

where

$$L_r = \sqrt{\left(\frac{x - x_c}{x_r}\right)^2 + \left(\frac{z - z_c}{z_r}\right)^2} \quad (67)$$

and the dimensions of the bubble are given (in metres) as $(x_c, x_r) = (0, 4000)$ and $(z_c, z_r) = (3000, 2000)$. Following Straka *et al.* (1993), and to obtain a solution that converges as the grid spacing is reduced, a constant viscosity term is added to the right-hand sides of the momentum equations (1)−(3) as well as to the thermodynamic equation (5). The viscosity term for a given prognostic variable, ϕ, takes the discrete form

$$\nu\left(\delta_x^2\phi + \delta_\eta^2\phi\right), \quad (68)$$

with $\nu = 75\,m^2\,s^{-1}$. This term is evaluated explicitly as a corrector step at the end of each time step, and

therefore leads to a viscous stability limit on the time step. The background initial atmosphere is isentropic and in hydrostatic balance with constant potential temperature $\theta^{ref} = 300\,K$. A representative subset of the grid resolutions of Straka *et al.* (1993) is used here, specifically 400, 200, 100, 50 and 25 m. The respective time steps are 4, 2, 1, 0.5 and 0.25 s. (Note that for the 25 m resolution, the time step is a factor of 16 larger than the value cited by Straka *et al.* (1993) as being used for their 25 m reference solution.) The solution is integrated to a time of 15 min. Results for different grid sizes at this time are shown in Figure 3 and the variations in the maximum and minimum values of $\Delta\theta$ (where $\Delta\theta \equiv \theta - 300\,K$), as well as the location of the front of the density current ($-1\,K$ contour) are summarized in Table II. The reference solution in the discussion below is taken to be the 25 m result of Straka *et al.* (1993).

With a resolution of 400 m, the features of the flow are very poorly resolved and this resolution is clearly inadequate to represent the scales of the flow in sufficient detail. This is consistent with the results of other authors, and is reflected in the fact that there are very large variations in the results from different models (see, for example figure 5(g)−(i) of Straka *et al.* (1993)) at this resolution. Increasing the resolution to 200 m significantly decreases the overshoot in the value of $\Delta\theta_{max}$ (which analytically should be 0 K) and a second rotor, which has a clearer correspondence to the second rotor of the reference solution, is now evident. For grid sizes of 100 m and less, a third rotor is apparent and also the front location is now well represented. Whilst differences are still visible between the 50 m and 25 m resolutions, the simulations are very close to being converged.

Comparing these results with the compressible reference solution of Straka *et al.* (1993) (their figure 3) it can be seen that for high resolutions (25−100 m) there is little difference between the results. The main difference is that here there is a more distinct separation between the rotors. This is most easily seen in the $-1\,K$ contour (the outermost, dark red contour) in Figures 3(d) and (e), which follows the outline of the rotors more closely than that in Straka *et al.* (1993) (this can be observed between the middle and rear rotor at $x \approx 10\,km$). In fact, at the highest resolution of 25 m, the $-1\,K$ contour completely encircles the rear rotor such that it is separated from the rest of the density current. Also, there is some distortion present in the lower part of the rear
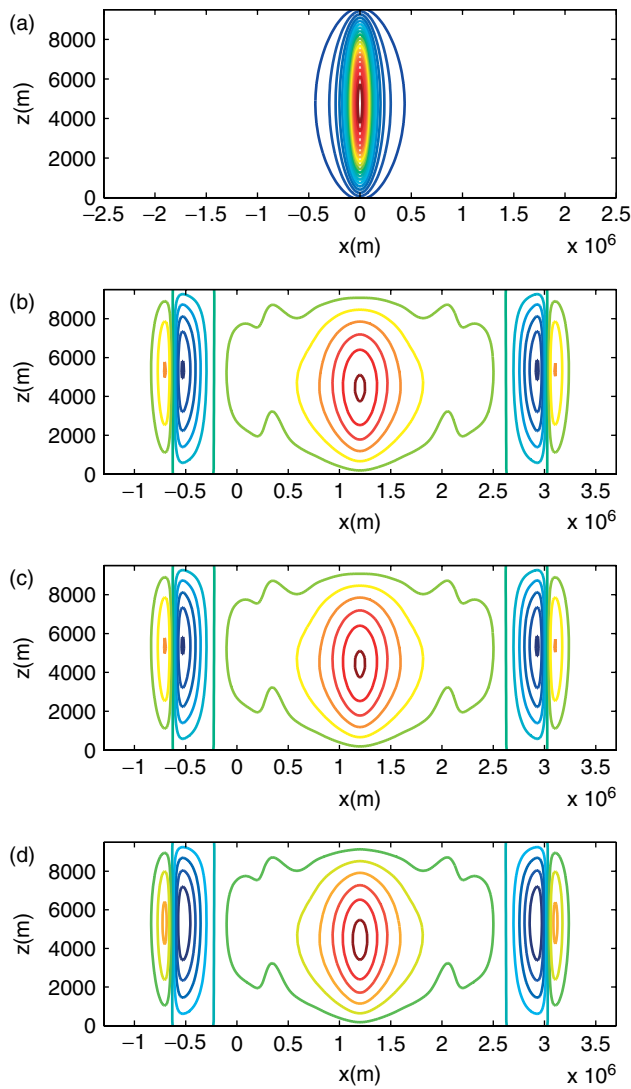
Figure 1. Hydrostatic inertia gravity waves. Panel (a) shows the initial θ perturbation. Panels (b), (c) and (d) show the perturbation at $t = 60\,000$ s for, respectively, the non-hydrostatic ($\delta_V = 1$) mass-conserving, non-hydrostatic ($\delta_V = 1$) standard SISL and hydrostatic ($\delta_V = 0$) mass-conserving models. In all cases the contours include, and are centred about, the zero contour and have intervals of 5×10^{-4} K.

rotor for the 100 m solution in Straka *et al.* (1993) that does not appear in Figure 3(c) and is also absent in the results of Skamarock and Klemp (2008) using a higher-order scheme (their figure 4).

Repeating this test using the standard SISL model produces visually indistinguishable results from those presented in Figure 3. The variations in the maximum and minimum values of $\Delta\theta$, as well as the location of the front of the density current (-1 K contour) are given in Table III. These are very close, particularly at high resolution, to the corresponding results for the mass-conserving model presented in Table II.

4.3. Linear hydrostatic/non-hydrostatic flow over a hill

In this test, hydrostatic and non-hydrostatic mountain waves are simulated. The hill profile is a witch-of-Agnesi curve
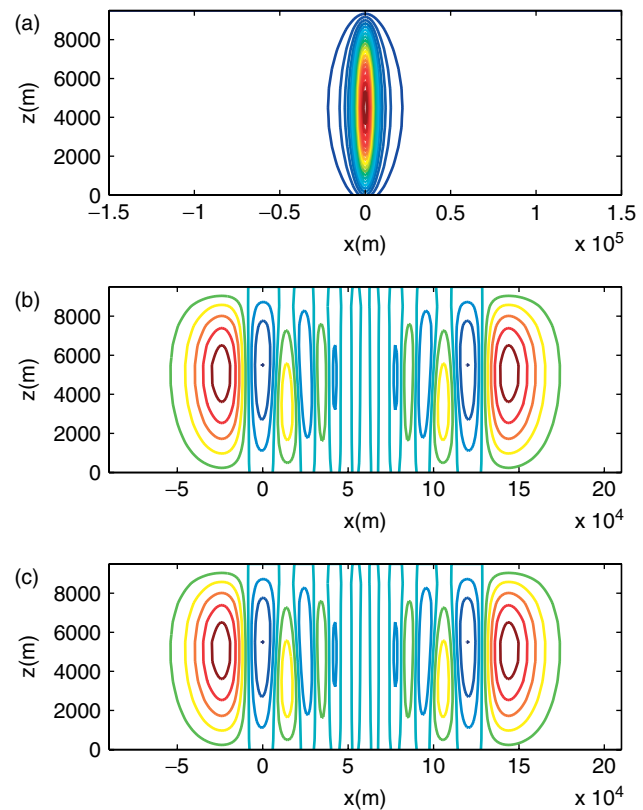
$$z_S(x) = \frac{h_m a^2}{x^2 + a^2}, \tag{69}$$

Figure 2. Non-hydrostatic gravity wave. Panel (a) shows the initial θ perturbation and panels (b) and (c) show perturbations at $t = 3000$ s for the non-hydrostatic mass-conserving and standard SISL models, respectively. In all the cases contours include, and are centred about, the zero contour and have intervals of 5×10^{-4} K.

Table II. Maximum and minimum values of $\Delta\theta$ as well as the location of the front of the density current after 15 min using the mass-conserving model with varying grid sizes.

Grid size (m)	$\Delta\theta_{min}$ (K)	$\Delta\theta_{max}$ (K)	Front location (m)
400	−5.6608	0.3674	13572
200	−8.0958	0.1226	14768
100	−9.8574	0.0995	15182
50	−9.4995	0.0626	15334
25	−9.6548	0.0048	15390

and a mean horizontal flow U is imposed. For the hydrostatic flow regime, a hill of height $h_m = 1$ m, half-width $a = 10$ km and mean wind speed of $U = 20$ m s^{-1} is used. The background initial state is isothermal with $T = 250$ K, and in hydrostatic balance. An absorbing layer is applied to the vertical momentum equation in the top 20 km of the domain with $\overline{\mu}\Delta t = 0.3$. For this case, the model has been run in both hydrostatic ($\delta_V = 0$) and non-hydrostatic ($\delta_V = 1$) modes.

In the non-hydrostatic flow regime, the hill half-width is reduced to $a = 1$ km and the mean wind speed is $U = 10$ m s^{-1}. The background initial state has constant buoyancy frequency $N = 0.01$ s^{-1} and therefore has finite depth. Due to this, the domain has a lower lid (35 km instead of 50 km as in the hydrostatic case) to prevent π^{ref} becoming negative. Therefore, the absorbing layer is only implemented in the top 10 km of the domain with $\overline{\mu}\Delta t = 0.15$.

Table III. As Table II but for the standard SISL model.

Grid size (m)	$\Delta\theta_{\min}$ (K)	$\Delta\theta_{\max}$ (K)	Front location (m)
400	-5.6027	0.3678	13551
200	-8.1021	0.1225	14756
100	-9.8504	0.0969	15179
50	-9.4997	0.0626	15334
25	-9.6550	0.0048	15390

Results for flow in the hydrostatic flow regime are shown in Figure 4. The results for the mass-conserving and standard SISL models are again indistinguishable from each other. The overall response in hydrostatic mode is very similar to that in non-hydrostatic mode, although the flow field is less uniform downstream of the waves, as observed in Figure 4(c) (cf. Figure 4(a) where the flow field is nearly uniform downstream of the waves).

It can be observed from Figure 4(a) and (b) that in the non-hydrostatic mode ($\delta_V = 1$) the waves tilt downstream in the positive x-direction, as in Klemp and Durran (1983) (their figure 2). Such a tilt is not present in the hydrostatic mode (Figure 4(c)), nor in the analytic linear hydrostatic solution (Figure 4(d)) but is present in the linear non-hydrostatic solution (Figure 4(e)). The Froude number ($Fr \equiv U/aN$) of these simulations is $Fr \approx 0.1$. Simulations (not shown) at a reduced Froude number, $Fr \approx 0.01$, show no such tilt. This all demonstrates that it is a non-hydrostatic effect, and not a nonlinear one or a numerical artefact.

Results for the non-hydrostatic flow regime are presented in Figure 5. There is again extremely good agreement between the mass-conserving and standard SISL models, with only very small differences of $\mathcal{O}\left(10^{-5}\mathrm{ms}^{-1}\right)$.

Figure 6 shows the same results as Figures 4(a) and 5(a) but with the Courant numbers increased from 0.2 (for the hydrostatic case) and 0.125 (for the non-hydrostatic case) to 1.5 (for both cases) and with $\overline{\mu}\Delta t$ held constant at 0.3 and 0.15 respectively. It is seen that the overall dynamics of the flow are still well captured for both the hydrostatic and non-hydrostatic flow regimes, although the increased Courant number leads to some distortion around the edges of the waves.

4.4.   Schär test

The Schär test case (Schär *et al.*, 2002) simulates flow over a hill comprising both small- and large-scale features. This presents a particularly challenging test for models employing a terrain-following coordinate (see Klemp *et al.* (2003), Girard *et al.* (2005) and the brief discussion in section 3.1.6). The orography is defined to be

$$z_S(x) = h_m \mathrm{e}^{-(x/a)^2} \cos^2\left(\frac{\Pi x}{\lambda}\right), \qquad (70)$$

where $h_m = 250\,\mathrm{m}$, $\lambda = 4\,\mathrm{km}$ and $a = 5\,\mathrm{km}$. The background initial state has constant buoyancy frequency $N = 0.01\,\mathrm{s}^{-1}$ and a mean wind of $U = 10\,\mathrm{m\,s}^{-1}$ is imposed. Two values of time step are used: $\Delta t = 8\,\mathrm{s}$ to compare with the results presented elsewhere in the literature, e.g. Schär *et al.* (2002), Klemp *et al.* (2003), and the five times larger value of $\Delta t = 40\,\mathrm{s}$ (corresponding to an increased Courant number of $C_x = 0.8$) to see how well the model performs
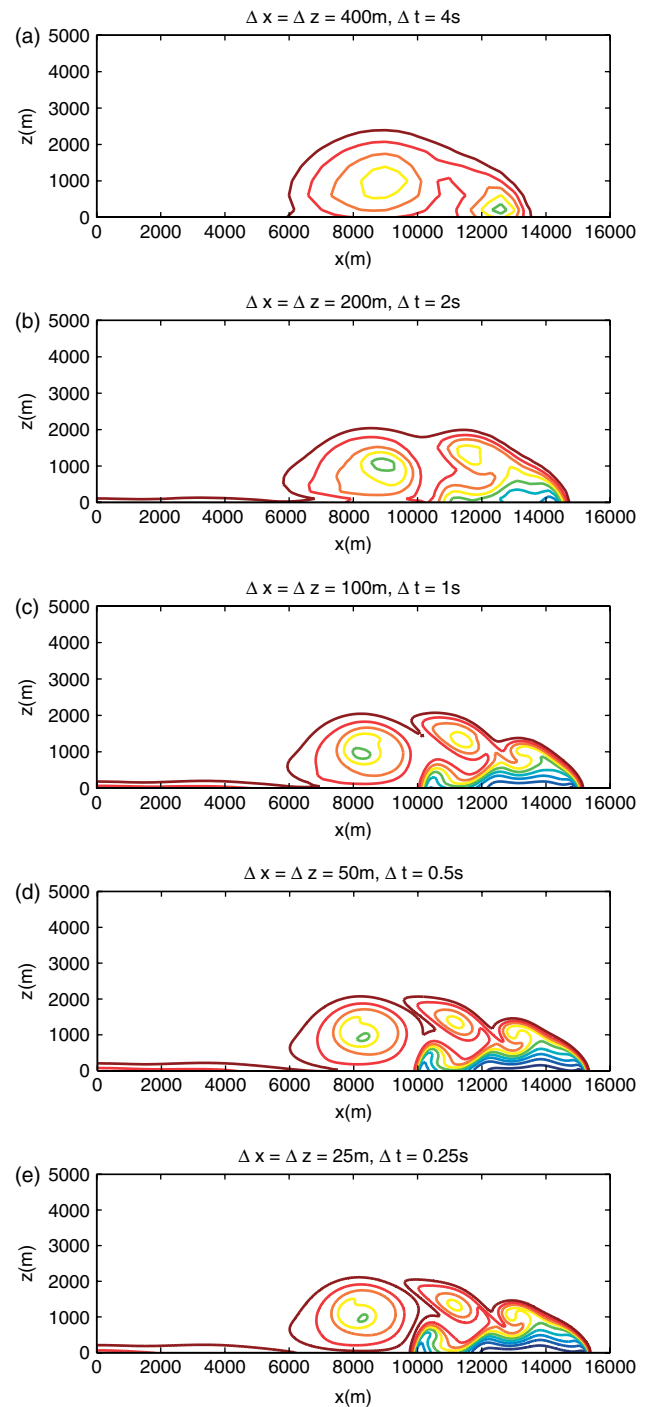
Figure 3. Potential temperature variation for the mass-conserving model after 15 min for 400, 200, 100, 50 and 25 m grids. Contour intervals are 1 K with the first contour being at -1 K.

at larger Courant numbers. Once again, to reduce the spurious effects of waves reflecting off the upper boundary, an absorbing layer is used in the top 10 km of the domain with $\overline{\mu}\Delta t = 1.2$ for both $\Delta t = 8\,\mathrm{s}$ and $\Delta t = 40\,\mathrm{s}$. The results for both mass-conserving and standard SISL models are shown in Figure 7. In both cases, the results (Figure 7(a) and (b)) are similar to the numerical result of Klemp *et al.* (2003) (see their figure 4(a)). Even with a much larger time step (Figure 7(c) and (d)) there is only a small deterioration in the smallest contour at the edges of the waves. The linear analytic solution (corresponding to that given in figure 1(a) of Klemp *et al.* (2003)) is shown in Figure 8. Whilst the
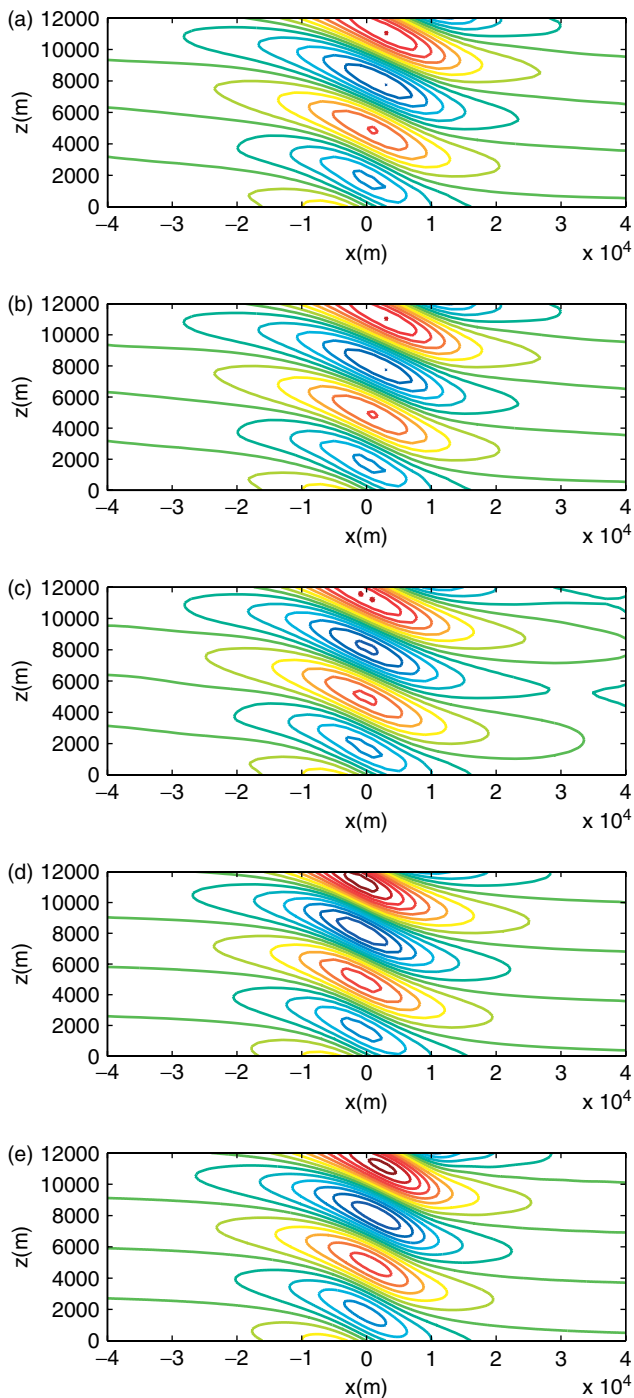
Figure 4. Vertical velocity, w, for the hydrostatic mountain-wave test after $Ut/a = 30 \Rightarrow t = 15\,000$ s: (a) mass-conserving model, (b) standard SISL model, (c) mass-conserving model in hydrostatic mode ($\delta_V = 0$) and linear analytic anelastic solutions (Smith, 1979) for (d) hydrostatic and (e) non-hydrostatic flows. Contour intervals are every 5×10^{-4} m s^{-1}.
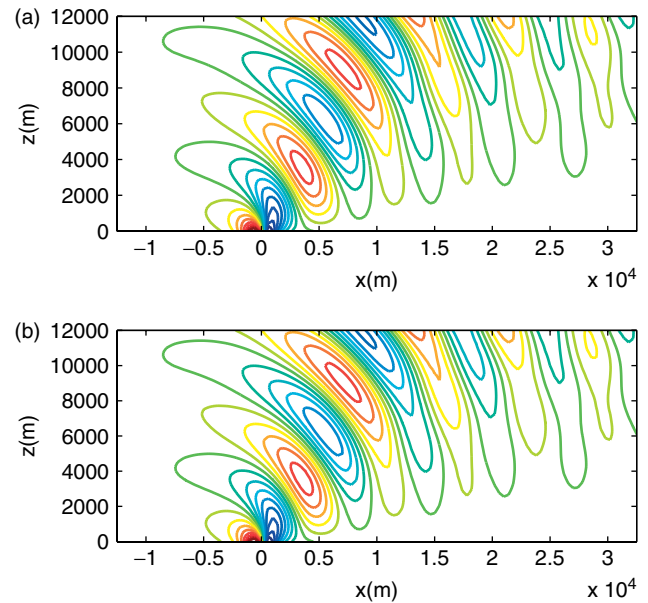

Figure 5. Vertical velocity, w, for the non-hydrostatic mountain-wave test, (a) mass-conserving model and (b) standard SISL model after $Ut/a = 45 \Rightarrow t = 9000$ s. Contour intervals are every 6×10^{-4} m s^{-1}.
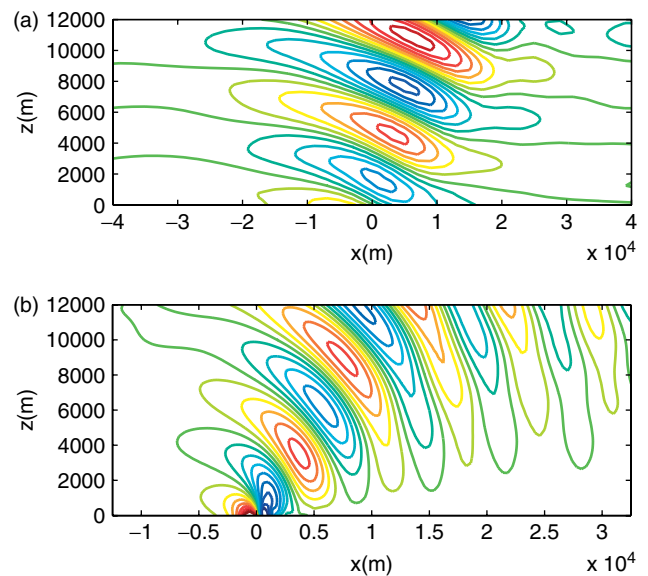

Figure 6. Vertical velocity profiles, w, for the mass-conserving model for (a) hydrostatic mountain waves (HMW) with increased Courant number $C_x = 1.5$ (with a corresponding time step $\Delta t = 150$ s) and (b) non-hydrostatic mountain waves (NHMW) with increased Courant Number $C_x = 1.5$ (with a corresponding time step $\Delta t = 60$ s). All other parameters are as in Figures 4 and 5.

overall pattern is very similar to that seen in Figure 7, there is a systematic increase in the magnitude of the vertical velocity in the nonlinear solution compared with the linear solution. This behaviour is similar to that observed in Klemp *et al.* (2003).

The virtue of using the consistent semi-Lagrangian discretization (37) of $\dot{\eta}$ is demonstrated by repeating the tests displayed in Figure 7 but using the standard Eulerian definition of $\dot{\eta}$ (B6), i.e. (37) is replaced with

$$\left[(\delta_\eta z)\,\dot{\eta} - w\right]_A^{n+1} = -\overline{\left(u_A^{n+1}\right)}^{x\eta} \delta_x z. \quad (71)$$

The impact of this can be clearly seen in Figure 9 where there is significant distortion of the waves, notably the distinct double maxima/minima in the structure of the large-scale waves (cf. Figure 7 where these spurious extrema are absent). Analysis by Klemp *et al.* (2003) showed that this Eulerian approach leads to a lack of cancellation in certain metric terms due to the terrain-following vertical coordinate used.

5. Conclusions

Following recent developments in a SWE model context, a method for stably coupling an inherently mass-conserving
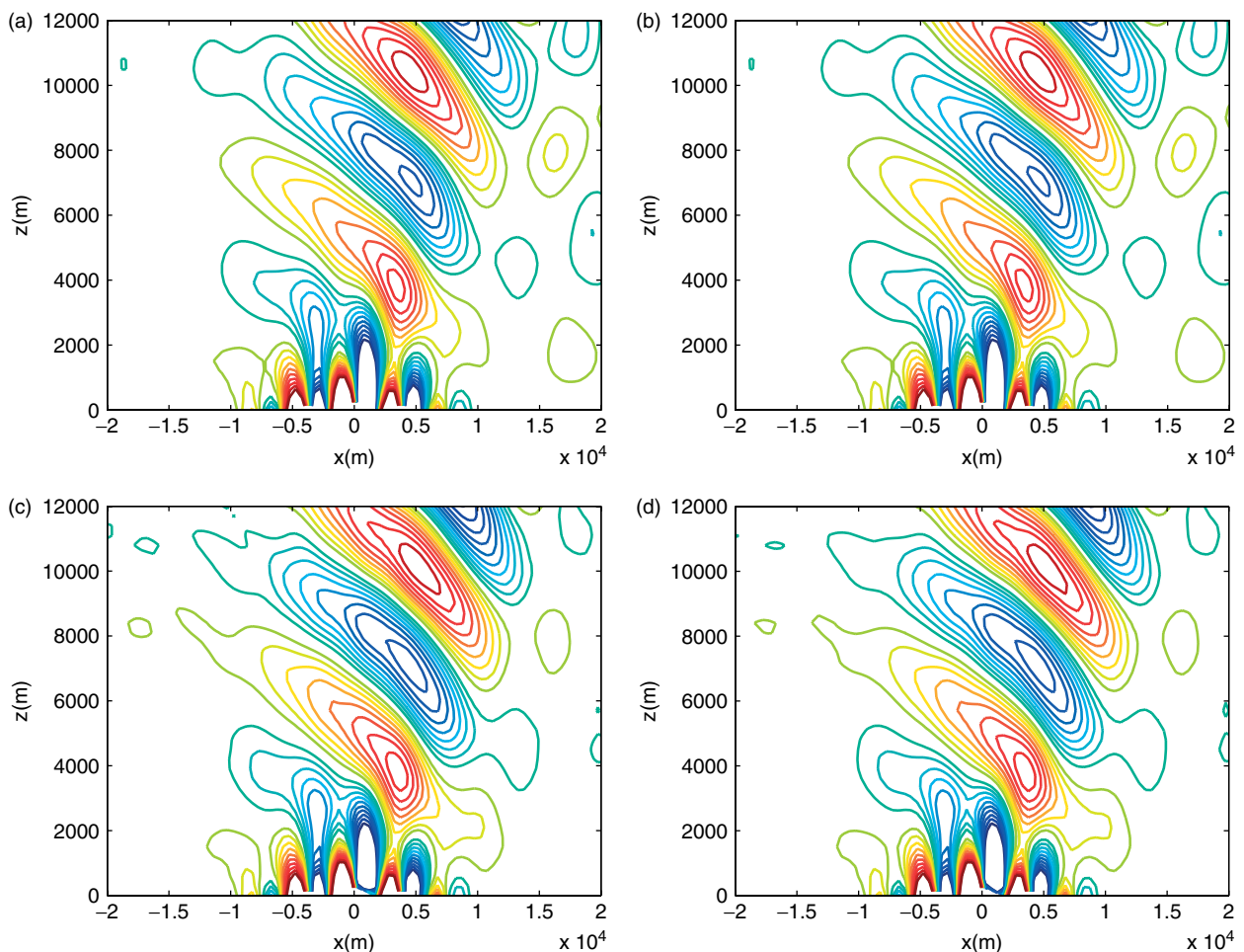
Figure 7. Vertical velocity profiles, w, for flow over a Schär hill after 5 hours. Panels (a) and (b) respectively show the mass-conserving and standard SISL models with $\Delta t = 8$ s. Panels (c) and (d) respectively show the mass-conserving and standard SISL models with $\Delta t = 40$ s. Contour intervals are every 5×10^{-2} m s^{-1}.
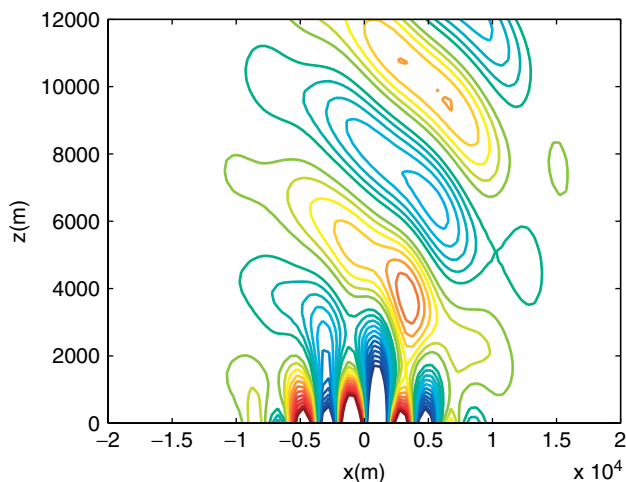

Figure 8. Linear analytic vertical velocity, w, profile of flow over a Schär hill.

semi-Lagrangian transport scheme to a semi-implicit discretization of the fully compressible, non-hydrostatic vertical-slice equations has been presented. The method of coupling allows a simple switch between the mass-conserving scheme and a standard non-mass-conserving SISL scheme, without the need for any structural changes to the model.

The model has been applied to a number of standard test cases from the literature, designed to exercise the various aspects of a vertical-slice model. In all cases the mass-conserving and standard SISL schemes have given very similar results, both to each other and to other published results.

The discretization brings together a number of features, in addition to its mass-conserving property. It is based on a multiply-nested iterative approach that at convergence and, for the values of off-centring parameters used here, gives a centred second-order SISL scheme with no three-time-level extrapolation. The model is therefore genuinely two-time-level. In order to give good wave dispersion properties and global energy conservation, the discretization of the Coriolis terms is based on an extension of that of Thuburn and Staniforth (2004). For a semi-Lagrangian finite-volume-based scheme, such as SLICE, it is important that the departure control volume is not vanishingly small. Therefore, the near boundary correction of Wood *et al.* (2009) has been applied to the departure points to avoid them lying spuriously at or beyond a physical boundary. To control the spurious reflection of vertically propagating waves from the model lid, an absorbing layer has been implemented, motivated by the results of Klemp *et al.* (2008). Finally it has been demonstrated, here in a two-time-level context, how a SL discretization of the relation between the vertical velocity of the transformed grid and
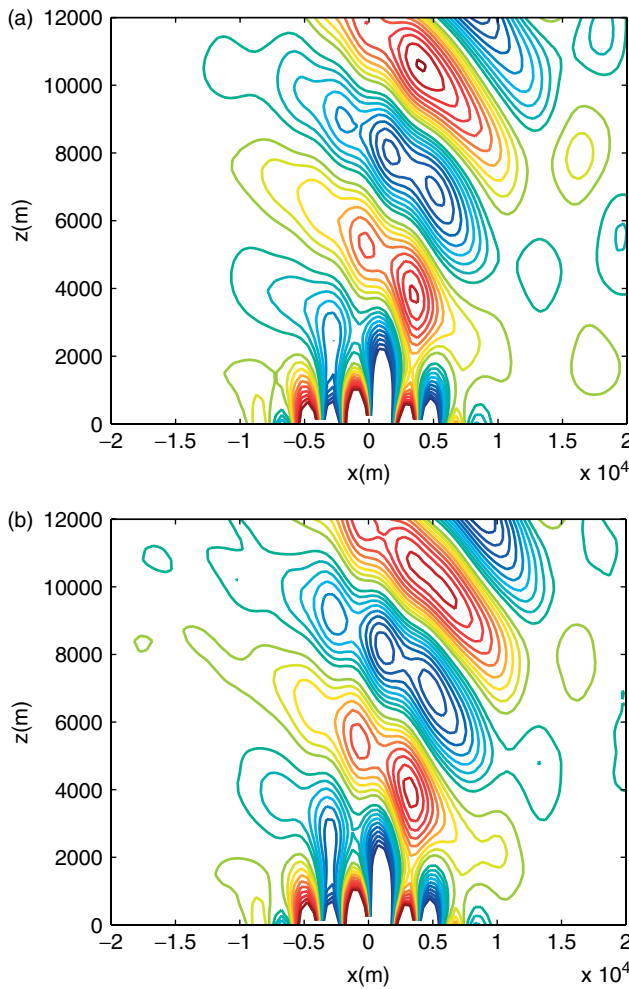
Figure 9. Vertical velocity, w, profiles of the mass-conserving model for flow over a Schär hill using the Eulerian definition of $\dot{\eta}$ (71), for (a) $\Delta t = 8$ s and (b) $\Delta t = 40$ s. All other parameters are as in Figure 7.

the actual vertical velocity gives significantly improved simulations of flow over fine-scale orography. This finding is consistent with, and motivated by, the analysis of Klemp *et al.* (2003) and the results of Girard *et al.* (2005), but has here been implemented in a centred two-time-level context rather than the three-time-level context of Girard *et al.* (2005).

The scheme presented here represents an extension of the work of Zerroukat *et al.* (2009) to the vertical to include non-hydrostatic effects and the influence of a terrain-following coordinate in the presence of orography. However, at the same time, it has simplified the geometry from being spherical, with the complications of coordinate poles (for a latitude–longitude grid) and non-degenerate Rossby-wave propagation, to Cartesian. It therefore remains for us to implement a fully three-dimensional version of the scheme on a sphere.

Acknowledgements

Appendix A: Introduction of reference-state terms into the continuity and thermodynamic equations

Subtracting and adding reference state terms, the continuity equation (4) can be rewritten as

$$
\begin{aligned}
0 &= \frac{D}{Dt}\left[\int_{\delta\mathcal{A}}\left(\rho - \rho^{\text{ref}}\right)d\mathcal{A}\right] + \frac{D}{Dt}\left(\int_{\delta\mathcal{A}}\rho^{\text{ref}}\,d\mathcal{A}\right) \\
&= \frac{D}{Dt}\left[\int_{\delta\mathcal{A}}\left(\rho - \rho^{\text{ref}}\right)d\mathcal{A}\right] + \int_{\delta\mathcal{A}}\frac{D\rho^{\text{ref}}}{Dt}\,d\mathcal{A} \\
&\quad + \int_{\delta\mathcal{A}}\rho^{\text{ref}}\frac{D}{Dt}\,(d\mathcal{A}) \\
&= \frac{D}{Dt}\left[\int_{\delta\mathcal{A}}\left(\rho - \rho^{\text{ref}}\right)d\mathcal{A}\right] + \int_{\delta\mathcal{A}}\mathbf{u}\cdot\nabla\rho^{\text{ref}}\,d\mathcal{A} \\
&\quad + \int_{\delta\mathcal{A}}\rho^{\text{ref}}\left(\nabla\cdot\mathbf{u}\right)d\mathcal{A} \\
&= \frac{D}{Dt}\left[\int_{\delta\mathcal{A}}\left(\rho - \rho^{\text{ref}}\right)d\mathcal{A}\right] \\
&\quad + \int_{\delta\mathcal{A}}\nabla\cdot\left(\rho^{\text{ref}}\mathbf{u}\right)d\mathcal{A},
\end{aligned}
\tag{A1}
$$

where, with the assumption that ρ^{ref} is independent of time, the identities

$$
\frac{D\rho^{\text{ref}}}{Dt} \equiv \mathbf{u}\cdot\nabla\rho^{\text{ref}}, \qquad \frac{D}{Dt}\,(d\mathcal{A}) \equiv (\nabla\cdot\mathbf{u})\,d\mathcal{A}
\tag{A2}
$$

have been used.

Subtracting and adding reference state terms, the thermodynamic equation (5) can be rewritten as

$$
0 = \frac{D}{Dt}\left(\theta - \theta^{\text{ref}}\right) + \frac{D\theta^{\text{ref}}}{Dt} = \frac{D}{Dt}\left(\theta - \theta^{\text{ref}}\right) + \mathbf{u}\cdot\nabla\theta^{\text{ref}},
\tag{A3}
$$

where θ^{ref} has been assumed independent of time.

Appendix B: Transformation relations

For a generic scalar G, the following transformation relations hold for $\psi = x$ or t:

$$
\left(\frac{\partial G}{\partial\psi}\right)_z = \left(\frac{\partial z}{\partial\eta}\right)^{-1}\left\{\frac{\partial}{\partial\psi}\left[\left(\frac{\partial z}{\partial\eta}\right)G\right]_\eta - \frac{\partial}{\partial\eta}\left[\left(\frac{\partial z}{\partial\psi}\right)_\eta G\right]_{x,t}\right\},
\tag{B1}
$$

$$
\left(\frac{\partial G}{\partial z}\right)_{x,t} = \left(\frac{\partial z}{\partial\eta}\right)^{-1}\left(\frac{\partial G}{\partial\eta}\right)_{x,t}.
\tag{B2}
$$

An alternative non-flux form version of (B1) is

$$
\left(\frac{\partial G}{\partial\psi}\right)_z = \left(\frac{\partial G}{\partial\psi}\right)_\eta - \left(\frac{\partial z}{\partial\psi}\right)_\eta\left(\frac{\partial z}{\partial\eta}\right)^{-1}\left(\frac{\partial G}{\partial\eta}\right)_{x,t}.
\tag{B3}
$$

Subscripts signify what is held constant whilst carrying out the operation contained within the associated parentheses. Henceforth, however, these subscripts are dropped for conciseness.

Using the transformation relations (B2) and (B3),

$$\mathbf{u} \cdot \nabla G = u\frac{\partial G}{\partial x} + \left(\frac{\partial z}{\partial \eta}\right)^{-1}\frac{\partial G}{\partial \eta}\left(w - u\frac{\partial z}{\partial x}\right). \quad \text{(B4)}$$

The Lagrangian derivative thus transforms to

$$\frac{DG}{Dt} \equiv \frac{\partial G}{\partial t} + u\frac{\partial G}{\partial x} + \left(\frac{\partial z}{\partial \eta}\right)^{-1}\left(w - u\frac{\partial z}{\partial x}\right)\frac{\partial G}{\partial \eta}. \quad \text{(B5)}$$

In particular,

$$\dot{\eta} \equiv \frac{D\eta}{Dt} = \left(\frac{\partial z}{\partial \eta}\right)^{-1}\left(w - u\frac{\partial z}{\partial x}\right), \quad \text{(B6)}$$

so that (B5) can be simplified and rewritten to give the expected form:

$$\frac{DG}{Dt} = \frac{\partial G}{\partial t} + u\frac{\partial G}{\partial x} + \dot{\eta}\frac{\partial G}{\partial \eta}. \quad \text{(B7)}$$

For motion that is constrained to be along surfaces of constant η, it follows that

$$\left.\frac{DG}{Dt}\right|_{\eta} = \frac{\partial G}{\partial t} + u\frac{\partial G}{\partial x}. \quad \text{(B8)}$$

Therefore (B7) can be rewritten as

$$\frac{DG}{Dt} = \left.\frac{DG}{Dt}\right|_{\eta} + \dot{\eta}\frac{\partial G}{\partial \eta}, \quad \text{(B9)}$$

and, in particular, for $G \equiv z$,

$$w \equiv \frac{Dz}{Dt} = \left.\frac{Dz}{Dt}\right|_{\eta} + \dot{\eta}\frac{\partial z}{\partial \eta}. \quad \text{(B10)}$$

Using now (B1) and (B2),

$$\nabla \cdot \mathbf{F} = \left(\frac{\partial z}{\partial \eta}\right)^{-1}\left[\frac{\partial}{\partial x}\left(\frac{\partial z}{\partial \eta}F_x\right) + \frac{\partial}{\partial \eta}\left(F_z - \frac{\partial z}{\partial x}F_x\right)\right], \quad \text{(B11)}$$

$$(\nabla G)_x = \left(\frac{\partial z}{\partial \eta}\right)^{-1}\left[\frac{\partial}{\partial x}\left(\frac{\partial z}{\partial \eta}G\right) - \frac{\partial}{\partial \eta}\left(\frac{\partial z}{\partial x}G\right)\right], \quad \text{(B12)}$$

$$(\nabla G)_z = \left(\frac{\partial z}{\partial \eta}\right)^{-1}\frac{\partial G}{\partial \eta}, \quad \text{(B13)}$$

$$d\mathcal{A} \equiv \frac{\partial z}{\partial \eta}\,dx\,d\eta. \quad \text{(B14)}$$

Appendix C: Variable placement and spatial operators

Let the domain $[x_0, x_I] \otimes [\eta_0, \eta_K] \equiv [-D/2, +D/2] \otimes [0, 1]$ be divided into I intervals $[x_{i-1}, x_i]$, $i = 1, 2, ..., I$ in the x direction, and K intervals $[\eta_{k-1}, \eta_k]$, $k = 1, 2, ..., K$ in the η direction. Then u points are located at $(x_i, \eta_{k-1/2})$, w, $\dot{\eta}$ and θ points at $(x_{i-1/2}, \eta_k)$ and v, ρ and π points at $(x_{i-1/2}, \eta_{k-1/2})$, where the half-integer coordinates are interleaved with the integer ones. z is held at any point where it is needed; see Figure C1 for details.

In what follows, the grid intervals are

$$\Delta x_l \equiv x_{l+\frac{1}{2}} - x_{l-\frac{1}{2}}, \qquad \Delta \eta_l \equiv \eta_{l+\frac{1}{2}} - \eta_{l-\frac{1}{2}}, \quad \text{(C1)}$$

where the grid index l is a positive integral multiple of $1/2$.

Averaging operators $\overline{G}^x$, $\overline{G}^\eta$, $\langle G \rangle^x$ and $\langle G \rangle^\eta$ are defined as

$$\overline{G}^x\big|_{i,k} \equiv \left(\frac{x_{i+\frac{1}{2}} - x_i}{\Delta x_i}\right)G_{i-\frac{1}{2},k} + \left(\frac{x_i - x_{i-\frac{1}{2}}}{\Delta x_i}\right)G_{i+\frac{1}{2},k}, \quad \text{(C2)}$$

$$\overline{G}^\eta\big|_{i,k} \equiv \left(\frac{\eta_{k+\frac{1}{2}} - \eta_k}{\Delta \eta_k}\right)G_{i,k-\frac{1}{2}} + \left(\frac{\eta_k - \eta_{k-\frac{1}{2}}}{\Delta \eta_k}\right)G_{i,k+\frac{1}{2}}, \quad \text{(C3)}$$

$$\langle G \rangle^x\big|_{i,k} \equiv \frac{1}{2}\left(G_{i-\frac{1}{2},k} + G_{i+\frac{1}{2},k}\right), \quad \text{(C4)}$$

$$\langle G \rangle^\eta\big|_{i,k} \equiv \frac{1}{2}\left(G_{i,k-\frac{1}{2}} + G_{i,k+\frac{1}{2}}\right), \quad \text{(C5)}$$

where i and k (both being positive, integral multiples of $1/2$) are the grid indices in the x and η directions, respectively, x_i denotes the value of x at the ith grid point in the x-direction and η_k denotes the value of η at the kth grid point in the η-direction. For a general variable, G, $G|_{i,k}$ denotes evaluation of G at the (i, k)th grid point.

Differencing operators $\delta_x G$ and $\delta_\eta G$ are defined as

$$(\delta_x G)_{i,k} \equiv \frac{G_{i+\frac{1}{2},k} - G_{i-\frac{1}{2},k}}{\Delta x_i}, \quad \text{(C6)}$$

$$(\delta_\eta G)_{i,k} \equiv \frac{G_{i,k+\frac{1}{2}} - G_{i,k-\frac{1}{2}}}{\Delta \eta_k}. \quad \text{(C7)}$$
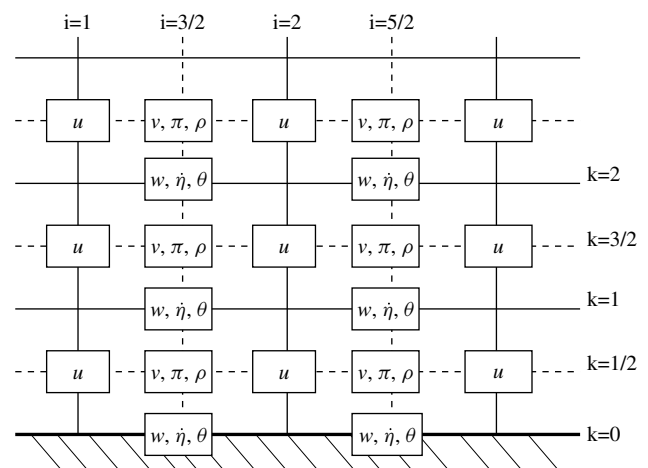

Figure C1. Placement of variables in the horizontal (i index) and the vertical (k index).

Appendix D: Algorithm for the iterative solution of the nonlinear coupled set of equations

Do $n = 1, N$ (begin time-step loop)
    −given the solution at time-level n, let this also be the first estimate for the time-level $n + 1$ solution
  Do $m = 1, M$ (departure (outer-loop) iteration)
      −compute the next estimate of the departure points (x_D, η_D) from (35)−(36), using $(u, \dot{\eta})_D^n$ and the latest estimate for $(u, \dot{\eta})^{n+1}$
      −evaluate $(R_u^n, R_v^n, R_w^n, R_\rho^n, R_\theta^n)$ at departure points using (24)−(26), (30) and (33)
      −evaluate $\mathfrak{R}^n$ using (54)
    Do $l = 1, L$ (non-linear (inner-loop) iteration)
        −evaluate $\left(R_u^*, R_v^*, R_w^*, R_\pi^*\right)$ using (47)−(50)
        −evaluate $\mathfrak{R}^*$ using (55), and then the right-hand side of (51)
        −solve the Helmholtz problem (51) for π' and hence obtain the next estimate for $\pi^{n+1} \equiv \pi^{\text{ref}} + \pi'$ at levels $k = 1/2, 3/2, .., K - 1/2$
        −obtain $\dot{\eta}^{n+1} \equiv \dot{\eta}'$ from (57) at levels $k = 1, 2, .., K - 1$ and set $\dot{\eta}^{n+1} \equiv \dot{\eta}' = 0$ on $k = 0$ and K
        −obtain θ' from (43), and hence obtain $\theta^{n+1} \equiv \theta^{\text{ref}} + \theta'$ at levels $k = 0, 1, 2, .., K$
        −obtain $w^{n+1} \equiv w'$ from (44) at levels $k = 1, 2, .., K - 1$
        −obtain $w_0^{n+1} \equiv w'$ from (44) with $\dot{\eta}'_0 = 0$, and set $w_K^{n+1} \equiv w'_K = 0$
        −obtain $u^{n+1} \equiv u'$ and $v^{n+1} \equiv v'$ from (39) and (40), respectively at levels $k = 1/2, 3/2, .., K - 1/2$
        −obtain ρ' from (42), and hence obtain $\rho^{n+1} \equiv \rho^{\text{ref}} + \rho'$ at levels $k = 1/2, 3/2, .., K - 1/2$
    Enddo
  Enddo
Enddo

Appendix E: Definitions of the Helmholtz coefficients

The definitions of the Helmholtz coefficients are

$$H_u \equiv \frac{\alpha \Delta t c_{\text{p}} \overline{\theta^{\text{ref}}}^{\eta}}{(\delta_\eta z)}, \tag{E1}$$

$$H_w \equiv \frac{\alpha \Delta t c_{\text{p}} \theta^{\text{ref}}}{(\delta_\eta z)}, \tag{E2}$$

$$H_{\rho x} \equiv (\delta_\eta z) \rho^{\text{ref}}, \tag{E3}$$

$$H_{\rho z} \equiv (\delta_\eta z) \overline{\rho^{\text{ref}}}^{\eta}, \tag{E4}$$

$$H_\theta \equiv \alpha \Delta t \delta_\eta \left(\overline{\theta^{\text{ref}}}^{\eta} \right), \tag{E5}$$

$$H_{\dot{\eta}} \equiv \delta_\eta z, \tag{E6}$$

$$H_V \equiv \frac{\alpha \Delta t \Delta x \Delta \eta}{\Delta \mathcal{A}}. \tag{E7}$$

References

Beckmann A, Diebels S. 1994. Effects of the horizontal component of the Earth's rotation on wave propagation on an f-plane. *Geophys. Astrophys. Fluid Dyn.* **76**: 95−119.

Côté J, Gravel S, Méthot A, Patoine A, Roch M, Staniforth A. 1998. The operational CMC−MRB Global Environmental Multiscale (GEM) model. Part I: Design considerations and formulation. *Mon. Weather Rev.* **126**: 1373−1395.

Davies T, Cullen M, Malcolm A, Mawson M, Staniforth A, White A, Wood N. 2005. A new dynamical core for the Met Office's global and regional modelling of the atmosphere. *Q. J. R. Meteorol. Soc.* **131**: 1759−1782.

Girard C, Benoit R, Desgagné M. 2005. Finescale topography and the MC2 dynamics kernel. *Mon. Weather Rev.* **133**: 1463−1477.

Hundertmark T, Reich S. 2007. A regularization approach for a vertical-slice model and semi-Lagrangian Störmer−Verlet time stepping. *Q. J. R. Meteorol. Soc.* **133**: 1575−1587.

Kaas E. 2008. A simple and efficient locally mass conserving semi-Lagrangian transport scheme. *Tellus A* **60**: 305−320.

Klemp JB, Durran DR. 1983. An upper boundary condition permitting internal gravity wave radiation in numerical mesoscale models. *Mon. Weather Rev.* **111**: 430−444.

Klemp JB, Skamarock WC, Fuhrer O. 2003. Numerical consistency of metric terms in terrain-following coordinates. *Mon. Weather Rev.* **131**: 1229−1239.

Klemp JB, Dudhia J, Hassiotis AD. 2008. An upper gravity-wave absorbing layer for NWP applications. *Mon. Weather Rev.* **136**: 3987−4004.

Lauritzen PH, Kaas E, Machenhauer B. 2006. A mass-conservative semi-implicit semi-Lagrangian limited-area shallow-water model on the sphere. *Mon. Weather Rev.* **134**: 1205−1221.

Lauritzen PH, Kaas E, Machenhauer B, Lindberg K. 2008. A mass-conservative version of the semi-implicit semi-Lagrangian HIRLAM. *Q. J. R. Meteorol. Soc.* **134**: 1583−1595.

Machenhauer B, Kaas E, Lauritzen PH. 2008. Finite-volume methods in meteorology. In *Handbook of Numerical Analysis: Special Volume on Computational Methods for the Atmosphere and the Oceans*, Ciarlet PG, Temam R, Tribbia J (eds). Elsevier: New York; pp. 3−120.

Reich S, Wood N, Staniforth A. 2007. Semi-implicit methods, nonlinear balance, and regularized equations. *Atmos. Sci. Letters* **8**: 1−6.

Schär C, Leuenberger D, Fuhrer O, Lüthi D, Girard C. 2002. A new terrain-following vertical coordinate formulation for atmospheric prediction models. *Mon. Weather Rev.* **130**: 2459−2480.

Shin S, Reich S. 2009. Hamiltonian particle-mesh simulations for a non-hydrostatic vertical slice model. *Atmos. Sci. Letters* **10**: 233−240.

Skamarock WC, Klemp JB. 1994. Efficiency and accuracy of the Klemp−Wilhelmson time-splitting technique. *Mon. Weather Rev.* **122**: 2623−2630.

Skamarock W, Klemp J. 2008. A time-split non-hydrostatic atmospheric model for weather research and forecasting applications. *J. Comput. Phys.* **227**: 3465−3485.

Smith RB. 1979. The influence of mountains on the atmosphere. *Adv. Geophys.* **21**: 87−230.

Straka JM, Wilhelmson RB, Wicker LJ, Anderson JR, Droegemeier KK. 1993. Numerical solutions of a non-linear density current: A benchmark solution and comparisons. *Int. J. Numer. Methods Fluids* **17**: 1−22.

Temam R, Tribbia J. 2003. Open boundary conditions for the primitive and Boussinesq equations. *J. Atmos. Sci.* **60**: 2647−2660.

Thuburn J, Staniforth A. 2004. Conservation and linear Rossby-mode dispersion on the spherical C grid. *Mon. Weather Rev.* **132**: 641−653.

Thuburn J, Woollings TJ. 2005. Vertical discretizations for compressible Euler equation atmospheric models giving optimal representation of normal modes. *J. Comput. Phys.* **203**: 386−404.

Thuburn J, Wood N, Staniforth A. 2002. Normal modes of deep atmospheres. II: $f − F$-plane geometry. *Q. J. R. Meteorol. Soc.* **128**: 1793−1806.

White AA, Hoskins BJ, Roulstone I, Staniforth A. 2005. Consistent approximate models of the global atmosphere: shallow, deep,

hydrostatic, quasi-hydrostatic and non-hydrostatic. *Q. J. R. Meteorol. Soc.* **131**: 2081–2107.

Wood N, Staniforth A, White AA. 2009. Determining near-boundary departure points in semi-Lagrangian models. *Q. J. R. Meteorol. Soc.* **135**: 1890–1896.

Zerroukat M, Wood N, Staniforth A. 2002. SLICE: A Semi-Lagrangian Inherently Conserving and Efficient scheme for transport problems. *Q. J. R. Meteorol. Soc.* **128**: 2801–2820.

Zerroukat M, Wood N, Staniforth A. 2006. The Parabolic Spline Method (PSM) for conservative transport problems. *Int. J. Numer. Methods Fluids* **11**: 1297–1318.

Zerroukat M, Wood N, Staniforth A. 2007. Application of the Parabolic Spline Method (PSM) to a multi-dimensional conservative transport scheme (SLICE). *J. Comput. Phys* **225**: 935–948.

Zerroukat M, Wood N, Staniforth A, White A, Thuburn J. 2009. An inherently mass-conserving semi-implicit semi-Lagrangian discretisation of the shallow water equations on the sphere. *Q. J. R. Meteorol. Soc.* **135**: 1104–1116.